Three-dimensional genome architecture connects chromatin structure and function in a major wheat pathogen

Ivona Glavincheska[1] and Cecile Lorrain[1*]

[1] Plant Pathology Group, Institute of Integrative Biology, ETH Zürich, Zürich, Switzerland

*Corresponding author: cecile.lorrain@usys.ethz.ch

ABSTRACT

Three-dimensional (3D) genome organization plays a central role in gene regulation and genome stability, yet its functional relevance in fungal pathogens remains largely uncharacterized. Here, we present a high-resolution Hi-C analysis of the wheat pathogen *Zymoseptoria tritici*, revealing a hierarchical genome organization. The genome adopts a Rabl-like conformation characterized by centromere clustering and the spatial segregation of accessory chromosomes, which remain tethered to core pericentromeres, supporting their mitotic stability. At finer resolution, we identify homotypic interactions among B compartments and self-interacting domains demarcated by distinct histone modifications and insulator-like sequence motifs at their boundaries. A subset of highly insulated domains enriched in heterochromatin and transposable elements engages in strong inter-domain interactions. During wheat infection, several self-interacting domains exhibit coordinated transcriptional activity, linking spatial genome folding to dynamic gene regulation. These findings uncover multi-scale principles of nuclear organization in a major fungal plant pathogen and establish a framework for investigating 3D genome function in filamentous fungi.

INTRODUCTION

The spatial organization of eukaryotic genomes is fundamental to cellular function, underpinning chromosomal dynamics, genome integrity, and the regulation of gene expression[1–3]. The physical arrangement of the chromatin in the nuclear space reflects a highly ordered and dynamic hierarchical architecture. Advances in chromosome conformation capture integrated with high-throughput sequencing (Hi-C) have significantly transformed our understanding of genome organization. In addition, Hi-C, combined with polymer physics models, can be used to differentiate between chromatin states and describe chromosomal conformation[4]. The comparison of 3D genome organization across the tree of life highlights both shared features and distinct aspects of genome organization between organisms, raising the question of whether common principles govern genome architecture[5].

In metazoan models, genome conformation studies have revealed a highly hierarchical chromatin organization[5]. At the largest scale, chromosomes are organized into distinct conformations within the nucleus, generally categorized into two main types: chromosome territory-like and Rabl-like organizations[2]. Chromosome territory-like organization, primarily observed in mammals, is characterized by minimal inter-chromosomal interactions, with each chromosome occupying a discrete nuclear region during interphase[2]. In contrast, the Rabl-like configuration involves a polarized arrangement where centromeres cluster at one end of the nucleus and telomeres align at the opposite end[2]. The Rabl chromosome configuration is also observed during mitosis[6]. Beyond these large-scale arrangements, epigenetically distinct compartments interact preferentially to further structure genome architecture[3,5,7]. In metazoans, A compartments correspond to transcriptionally active, euchromatic regions enriched in gene activity, while B compartments are associated with transcriptionally repressed, heterochromatic regions. This bipartite compartmentalization highlights the functional partitioning of the genome into regions of activity and repression. At a finer resolution, chromatin is organized into topologically

45 associating domains (TADs), self-interacting regions within which DNA sequences interact more
46 frequently than with sequences outside the domain[8]. The function of TADs remains debated, but they
47 have been described as playing an important role in regulating gene expression, partly by modulating the
48 interactions between regulatory elements and their target genes[9–11]. TAD boundaries act as insulators
49 that mediate chromatin looping to ensure proper genomic interactions and are enriched in architectural
50 proteins, such as the cohesin complex and the DNA-binding protein CCCTC-binding factor (CTCF), as well
51 as regions containing highly transcribed housekeeping genes[9]. The disruption of genome folding can
52 disrupt interactions between genes and regulatory elements, as observed in the enhancer hijacking of
53 proto-oncogenes[10,11]. In contrast to metazoan systems, other organisms exhibit 3D genome organization
54 patterns that, although reminiscent of features such as loops and compartments observed in mammals,
55 arise through distinct mechanisms. For instance, plants' compartment-like structures and Polycomb-
56 associated domains have been identified in gene-rich regions[12–15]. However, these domains are not
57 necessarily conserved across plant species and are not strongly associated with gene co-regulation as seen
58 in animals[15]. Understanding the establishment and regulatory impact of 3D genome organization is
59 essential. Yet, despite significant progress in metazoan models, these processes remain poorly
60 understood in many other eukaryotes, particularly in fungi.
61
62 The fungal kingdom, comprising millions of species, has significant ecological and economic impacts[16]. The
63 deployment of Hi-C sequencing has reshaped our understanding of fungal genome organization[17]. While
64 Hi-C has been widely applied to generate chromosome-level assemblies, high-resolution datasets remain
65 scarce for most fungal species, limiting our insights into their nuclear architecture[17]. Fungal genomes
66 generally exhibit a Rabl-like organization characterized by centromere clustering, as demonstrated in
67 yeast and filamentous fungi[17,18]. However, chromatin compartmentalization in fungi appears to be less
68 defined compared to that in metazoans. For instance, *Rhizophagus irregularis* is one of the few fungal

69 species with described A/B compartments[19]. TAD-like structures have also been identified in various fungi,
70 resembling metazoan TADs but with a notably smaller size. Although Hi-C matrices have revealed the
71 presence of TAD-like structures in fungal genomes, boundary-associated proteins potentially responsible
72 for domain insulation have yet to be identified. In the budding yeast *Saccharomyces cerevisiae*, interacting
73 domains of 5-10 kb depend on nucleosome positioning that create rigid chromatin segments that can
74 function as domain boundaries independently of architectural proteins[20]. In *S. cerevisiae*, these
75 interaction domains or TAD-like structures are implicated in critical genome functions such as
76 recombination repression, genome evolution, and the temporal organization of replication origins during
77 mitosis[20]. In the filamentous pathogen *Verticilium dahliae,* TAD-like structures exhibited strong internal
78 chromatin interactions and limited interactions beyond their boundaries, indicating roles in regulating
79 gene expression and maintaining chromosomal organization[21]. In *Neurospora crassa*, TAD-like structures
80 consist of weakly insulated euchromatic regions flanked by constitutive heterochromatin borders[22,23]. The
81 diverse chromatin organization observed across fungal species underscores the need for high-resolution
82 Hi-C to elucidate the fundamental principles of nuclear architecture and its influence on genome function.

83 The fungal wheat pathogen *Zymoseptoria tritici* emerged alongside the domestication of wheat in the
84 Fertile Crescent[24]. The genome of *Z. tritici* is compartmentalized into thirteen core and eight accessory
85 chromosomes[25,26]. The core chromosomes, which are gene-rich and transposable element (TE)-poor,
86 contrast with the gene-poor and TE-rich accessory chromosomes, an ancestral feature shared across the
87 *Zymoseptoria* genus[26]. The accessory chromosomes exhibit a high degree of presence/absence
88 polymorphism in *Z. tritici* populations[27], and some chromosomes appear to be more prone to
89 destabilization than others, as indicated by targeted loss experiments[28]. The genomic partitioning of *Z.*
90 *tritici* is further reflected by distinct epigenetic signatures, particularly in the presence of specific histone
91 modifications in accessory chromosomes[29]. The epigenetic landscape of *Z. tritici* exhibits the distinction
92 of euchromatin, constitutive and facultative heterochromatin, cytosine methylation (5mC) regions, small

93 acrocentric centromeres, and telomeric repeats, underlining the complexity of *Z. tritici*'s chromatin
94 organization[26,30–35]. Pathogenicity-related genes in *Z. tritici* are enriched within TE-rich regions of the
95 genome, which likely facilitates rapid evolution through genome rearrangements and epigenetic
96 regulation[35,36]. These genes are predominantly repressed in the absence of the host and maintained in a
97 transcriptionally silent state by heterochromatin marks[36]. Upon host colonization, chromatin remodeling
98 events activate the expression of pathogenicity-related genes[36]. Despite these detailed insights into the
99 genomic and epigenomic features of *Z. tritici*, the spatial organization of its genome and how these regions
100 fold and interact in three-dimensional space remains unexplored. This study aims to bridge this gap by
101 integrating high-resolution Hi-C to explore the 3D architecture of *Z. tritici*'s genome. To examine the
102 association between the epigenetic landscape and chromatin folding, we investigated the interplay
103 among genomic, epigenomic, and transcriptomic features, shedding light on the structural and regulatory
104 mechanisms that govern the genome of this major wheat pathogen.

105 # RESULTS

106 **The Rabl-like genome of *Z. tritici* reveals distinct conformation patterns between core and accessory**
107 **chromosomes**
108
109 To investigate the three-dimensional (3D) genome organization of *Z. tritici* IPO323, we performed Hi-C on
110 two independent replicates (Supplementary Fig. S1A). Quality control analysis confirmed reproducibility
111 between replicates, with a Pearson correlation of 0.87 and 77–81% valid read pairs per replicate
112 (Supplementary Fig. S1B). We combined the two datasets to generate a high-resolution contact map
113 containing ~19.2 million deduplicated valid read pairs (Supplementary Table S1), allowing us to resolve
114 chromatin interactions at a minimal bin size of 3 kb. At this resolution, 80% of bins in the core
115 chromosomes were covered by at least 1,000 contacts (Fig. 1A; Supplementary Table S2). At 10 kb
116 resolution, all chromosomes except chromosome 21 had at least 1,000 contacts in 90% of bins

117 (Supplementary Table S2). As expected, the Hi-C contact matrix was dominated by local interactions,
118 reflected by a strong signal along the diagonal of the genome-wide contact map (Fig. 1A). The strongest
119 interchromosomal contacts were enriched at centromeres and pericentromeric regions, consistent with
120 a Rabl-like conformation (observed-to-expected contact > 3.5; Fig. 1A, 1B; Supplementary Fig. S2-S3).
121 Strong interchromosomal interactions were predominantly enriched in regions marked by constitutive
122 heterochromatin (H3K9me3; Supplementary Fig. S3; Supplementary Table S3). Notably, 32.6% of the
123 strong interchromosomal interactions (observed-to-expected contact > 3.5) occurred between two
124 H3K9me3-enriched blocks, revealing a heterochromatin network spanning multiple chromosomes
125 (Supplementary Fig. S3C).
126
127 Accessory chromosomes preferentially anchored to the pericentromeric regions of core chromosomes,
128 with 78.6% of core-accessory interactions spanning the full length of accessory chromosomes but
129 restricted to the pericentromeric regions of core chromosomes (observed-to-expected contact > 3.5; Fig.
130 1B; Supplementary Fig. S3D). This spatial organization suggests that entire accessory chromosomes
131 primarily interact with core chromosomes at their centromeres and short arms while remaining
132 segregated from the long core chromosome arms (Fig. 1B). As accessory chromosome stability is variable,
133 we examined the potential relationship between chromosome loss and core-accessory pericentromeric
134 interaction strength[28]. We performed a log-transformed Poisson regression, which revealed a significant
135 negative association between interaction strength normalized for accessory chromosome size and the
136 loss frequency of accessory chromosomes in IPO323 after β-tubulin inhibition treatment[28] ($p = 5.33e-05$
137 for the intercept; $p = 0.0025$ for normalized interaction strength; Figure S4). This negative correlation
138 suggests a link between core-accessory interactions and the stability of accessory chromosome
139 transmission. Overall, we uncovered the Rabl-like structure of the *Z. tritici* IPO323 genome characterized
140 by interchromosomal interactions between (peri)centromeric regions and a heterochromatin-enriched

141 interaction network that possibly contributes to the spatial organization of the genome and maintains the
142 nuclear positioning of accessory chromosomes.
143
144 To determine whether chromatin conformation of core and accessory chromosomes is reflected by
145 distinct contact frequency decay values, we estimated the frequency decay exponent (α) as a function of
146 genomic separation and contact frequency for each chromosome. Here, the core chromosomes exhibited
147 an average decay exponent of α = -1.22 (standard deviation (SD) = 0.1), with three distinct scaling regimes
148 depending on genomic separation, indicating a hierarchical structure of the chromatin (Fig. 1C;
149 Supplementary Table S4). At short distances (< 70 kb), contact frequency decayed more gradually than
150 the global average with α = -0.71 (SD = 0.01). Interactions between 70 kb and 1 Mb followed a more
151 heterogeneous and steeper decline with α = -1.43 (SD = 0.09). At distances beyond 1 Mb, contact
152 frequency declined at a slower rate relative to intermediate distances (α = -1; SD = 0.09; Fig. 1C;
153 Supplementary Table S4). In contrast, accessory chromosomes displayed a more uniform decay of contact
154 frequency, with a global exponent of α = -0.67 (SD = 0.08; Fig. 1C; Supplementary Table S4). The contact
155 frequency decay was steepest at distances within 70 kb (α = -0.71; SD=0.18), and followed a shallower
156 decline at distances > 70 kb (α = -0.62; SD=0.01). This pattern suggests accessory chromosomes function
157 as unitary compartments and lack multiple self-interacting domains (Fig. 1C; Supplementary Table S4).
158 Together, these findings highlight a distinction in chromatin folding between core and accessory
159 chromosomes: core chromosomes display hierarchical folding and distance-dependent structural
160 transitions indicating the presence of self-interacting domains, whereas accessory chromosomes maintain
161 a more uniform and potentially less constrained conformation.

162 **B chromatin compartments in *Z. tritici* engage in homotypic interactions at the intrachromosomal level**

163 To further investigate the segregation of *Z. tritici* chromatin, we inferred compartmentalization strength
164 based on principal component analyses (PCA) of intrachromosomal contact matrices at 10 kb and 3 kb
165 resolution bins (Fig. 2; Supplementary Fig. S4). At 10 kb bins, eigenvector values segregated the
166 chromosome (sub)telomeres, supporting inter-arm interactions. At 3 kb, however, a finer distinction
167 between interaction patterns was present with negative eigenvector values associated with H3K9me3
168 enrichment regions (Supplementary Fig. S5). Compartmentalization strength at 3 kb bins was assessed by
169 comparing interaction frequencies between regions with similar (positive-positive or negative-negative)
170 and opposing (positive-negative) eigenvector values (Fig. 2A; Supplementary Fig. S5, S6). Regions with
171 negative eigenvectors exhibited stronger interactions (interaction strength = 2) than positive eigenvector
172 regions (interaction strength = 1; Fig. 2A; Supplementary Table S5). These negative eigenvector regions
173 were enriched with heterochromatin-associated histone modifications, particularly H3K9me2 and
174 H3K9me3, while depleted in euchromatin-associated H3K4me2, consistent with the characteristics of
175 canonical B-compartments seen in metazoans (Fig. 2B, Supplementary Fig. S6). The B-compartment blocks
176 had an average size of ~60 kb, accounting for 14.74 Mb (~36%) of the genome, and are characterized by
177 low gene density and a high density of TEs (Fig. 2C-D, Supplementary Table S6). Notably, we observed a
178 significant enrichment of retrotransposons, particularly LINEs and LTR elements from the *Copia*
179 superfamily (Fig. 2C-E, Supplementary Table S7).

180 By contrast, positive eigenvector regions were associated with characteristic features of A-compartments.
181 The A-compartment blocks had an average length of 100 kb, spanning a total of 24.35 Mb, of which 80.3%
182 are covered by genes (9,996 genes), while TEs made up only 4.6% of the A-compartment blocks (Fig. 2C).
183 These regions exhibited significantly higher gene density and lower TE density than B-compartment blocks
184 (Fig. 2D). Gene ontology (GO) enrichment analysis revealed an overrepresentation of functions related to
185 translation, ribosome function, RNA binding, and intracellular non-membrane-bounded organelles (FDR-

186 adjusted $p < 0.01$), suggesting a functional link to essential cellular processes such as protein biosynthesis,
187 RNA stability, modification, and transport (Supplementary Table S8-S9). Additionally, A-compartments
188 were enriched in non-autonomous miniature inverted-repeat elements (MITEs; Fig. 2E). Consistent with
189 these observations, genes and TEs within A-compartment blocks exhibited significantly higher *in vitro*
190 expression than those in B-compartment blocks (Fig. 2E), indicating that transcriptional regulation of both
191 genes and TEs is dependent on chromatin compartmentalization. The identification of intrachromosomal
192 A/B compartment blocks demonstrates that chromatin organization in *Z. tritici* goes beyond the global
193 distinction between core and accessory chromosomes.

194 **The presence of TAD-like organization in *Z. tritici* reveals boundaries enriched in facultative**
195 **heterochromatin and specific DNA binding motifs**

196 To investigate the presence of TAD-like structures in the *Z. tritici* IPO323 genome, we analyzed insulation
197 scores calculated from a 3 kb resolution Hi-C contact matrix. We identified 513 TADs and 533 TAD
198 boundaries in *Z. tritici* IPO323, with an average TAD length of approximately 70 kb (Supplementary Table
199 S10-12). The distribution of TADs varied between core and accessory chromosomes, with 92% of TADs
200 (473 TADs) located on core chromosomes and only 8% (40 TADs) on accessory chromosomes
201 (Supplementary Table S12). On average, TADs on core chromosomes contained 25 genes and 6 TEs,
202 whereas TADs on accessory chromosomes contained an average of 14 genes and 17 TEs per TAD
203 (Supplementary Table S12).

204 Since TAD boundaries act as insulators between TADs, we identified them by detecting local insulation
205 minima and further examined whether TAD boundaries exhibited specific epigenomic and genomic
206 features (Fig. 3A, 3B). We observed that TAD boundaries were depleted of the constitutive
207 heterochromatin histone modifications H3K9me2 and H3K9me3 but enriched for facultative
208 heterochromatin modifications H3K36me3, H4K20me1, and H4K20me3 (Fig. 3B, Supplementary Fig. S7).

209 In accessory chromosomes, TAD boundaries were also enriched for accessory chromosome-associated
210 modifications, H3K27me2 and H3K27me3 (Supplementary Fig. S7). In addition, TAD boundaries exhibited
211 a lower density of TEs, reduced RIP-like signatures, and a higher density of genes than TADs (Fig. 3B,
212 Supplementary Fig. S7). The active transcription mark H3K4me2, however, did not show a pattern of
213 enrichment at TAD boundaries (Supplementary Fig. S7). These findings indicate that TAD boundaries are
214 typically depleted in constitutive heterochromatin and enriched in facultative heterochromatin.

215 To investigate if TAD boundaries could be associated with housekeeping and core gene functions, such as
216 transcription factors and regulators, we first investigated the features of the 613 genes overlapping >50%
217 with TAD boundaries, including conservation across 19 *Z. tritici* strains[37], functional annotation
218 enrichment, and expression *in vitro* (Supplementary Table S11). We detected only 69 core genes with
219 orthologs in all 19 *Z. tritici* reference genomes (Fisher's test, p-value = 0.76; Supplementary Tables S13-
220 S15). Similarly, we did not find enrichment of specific Gene Ontology (GO) terms or functional domains
221 (Supplementary Tables S13-S15), nor did genes at boundaries exhibit differences in *in vitro* expression
222 levels compared to TAD-associated genes (Supplementary Fig. S8). Finally, we searched whether specific
223 DNA binding motifs were present at TAD boundaries and identified a significant enrichment of 35 known
224 and novel DNA binding motifs, grouped in 9 clusters (Supplementary Table S16). Interestingly, one of the
225 strongest matches showed similarity to the binding motif recognized by the mammalian KRAB zinc finger
226 protein, ZNF263. ZNF263 was recently shown to function as an insulating factor at TAD boundaries[38].
227 IPO323 has a single annotated KRAB zinc finger protein (ZtIPO323_082310), but this protein exhibits low
228 sequence similarity in its zinc finger domains with the human ZNF263 protein (Supplementary Table S17).
229 These results suggest that TAD boundaries in *Z. tritici* exhibit distinct epigenetic features and may
230 incorporate DNA binding motifs that are potentially recognized by insulator proteins.

231 **Highly insulated TADs define chromosomal conformation, while local TAD organization regulates**
232 **transcriptional dynamics during plant infection**

233 The analysis of the intrachromosomal contact matrix revealed heterogeneity in contact patterns across
234 TADs, with certain TADs exhibiting strong insulation to their proximal neighbors, indicative of a
235 compartmentalized chromatin environment (Fig. 3C-D). These TADs were characterized by elevated
236 insulation scores and flanked by lower insulation regions, suggesting stronger local boundaries. To further
237 investigate, we defined these highly insulated TADs (HI-TADs) by comparing the maximum insulation score
238 within each TAD to the scores of its boundaries (Fig. 3D). TADs with a sum of boundary-to-maximum
239 insulation scores above the genome-wide median were classified as HI-TADs. We identified 105 HI-TADs
240 across the genome, representing 20% of the total TADs (Supplementary Table S18). Analysis of strongest
241 interactions (observed-to-expected intrachromosomal contacts > 1.75) revealed significantly higher
242 strong intrachromosomal interactions between HI-TADs compared to R-TAD/R-TAD and HI-TAD/R-TAD
243 interactions (Mann-Whitney $p < 0.05$; Supplementary Fig. S9). HI-TADs displayed a unique epigenetic
244 profile, with strong enrichment for heterochromatin-associated marks H3K9me2 and H3K9me3 and
245 depletion of all other histone modifications (Fig. 3C–D). Of the 105 HI-TADs identified, 64% (68) were
246 associated with B-compartments. HI-TADs exhibited higher Repeat-Induced Point Mutation (RIP) indices,
247 increased TE density, and lower gene density than regular TADs. In addition, we observed that R-TADs
248 have significantly higher gene expression levels *in vitro* than HI-TADs (Supplementary Fig. S10). HI-TADs
249 were also enriched in effector genes, implying that heterochromatin dynamics within these regions may
250 be restructured to enable effector gene activation during host infection (Fisher's exact p-value < 0.01;
251 odds ratio = 1.54; Supplementary Tables S19). Taken together, these results suggest that HI-TADs
252 represent interspersed heterochromatic islands that may contain genes relevant for pathogenicity.

253 To investigate whether TADs function as co-regulatory domains in *Z. tritici*, we analyzed transcriptomic
254 data from axenic culture and wheat infection. Using a linear model, we investigated whether genes and
255 TEs within the same TAD were differentially coexpressed. We classified a TAD as co-regulated if at least
256 10 genes and TEs exhibited coordinated transcriptional changes (Supplementary Tables S20-23). The TAD
257 organization had a significant impact on gene expression dynamics between *in vitro* and *in planta*
258 conditions, with the model outperforming the null expectation in explaining transcriptional variation at
259 different infection stages and accounting for between 5%-9% of the adjusted variance in log fold-change
260 (likelihood ratio test $p < 0.01$; Supplementary Table S24). In addition, we performed further linear
261 regression analyses using TAD membership, gene GC content, and distance to the nearest TE as predictors
262 to determine whether other factors linked to gene expression can further explain transcriptional variation.
263 Adding both gene GC content and distance to nearest TE to the linear regression model explained an
264 additional 3-6% of the variance (Supplementary Table S24). However, in the absence of TAD membership
265 as a predictor variable gene GC content and TE distance only explained <0.1% of the transcriptional
266 variance. We identified 46 co-regulated TADs (8.9% of all TADs) with significant transcriptional
267 coordination during at least one stage of infection (Supplementary Fig. S11; Supplementary Table S25).
268 Interestingly, different TADs showed stage-specific co-expression patterns, with 23 co-regulated TADs
269 identified at only a single infection stage, reflecting localized chromatin dynamics between biotrophic and
270 necrotrophic phases of infection (Supplementary Fig. S11). We identified 19 co-regulated TADs in the
271 accessory chromosomes and six localized to the arm of chromosome 7, which display accessory
272 chromosome features, including H3K27me3 enrichment and sparse gene content (Supplementary Fig.
273 S12). Another third of co-regulated TADs are classified as HI-TADs (16 TADs). Collectively, these results
274 highlight that specific TADs act as functional modules of transcriptional regulation in *Z. tritici*, with regions
275 associated with heterochromatin, low gene density, and accessory features showing a greater
276 dependency on domain organization for coordinated gene expression.

277 # DISCUSSION

278 Our study provides the first comprehensive characterization of the hierarchical 3D chromatin organization
279 in the major fungal wheat pathogen *Z. tritici*. The genome of *Z. tritici* adopts a Rabl-like nuclear
280 conformation, consistent with other fungal genomes[19,21,23,39,40] but with distinct folding patterns between
281 core and accessory chromosomes. Accessory chromosomes are anchored to the pericentromeric regions
282 of core chromosomes, with interaction strength correlating with stability, indicating that pericentromeric
283 association may reinforce their nuclear positioning and stability. We detected hierarchical folding within
284 core chromosomes, while accessory chromosomes displayed a more uniform organization. Beyond this
285 global architecture, we identified intrachromosomal compartments, with B compartments engaging in
286 homotypic interactions and enriched for retrotransposons. Furthermore, we detected self-interacting
287 TAD-like structures with boundaries enriched in active chromatin marks and putative insulator motifs that
288 resemble the binding sites of a mammalian architectural protein. Additionally, we defined highly insulated
289 TADs that form an interaction network of heterochromatic islands and harbor genes related to
290 pathogenicity. A subset of TADs showed transcriptional co-regulation patterns that varied across infection
291 stages, indicating a regulatory role for TAD organization in infection stage-specific gene expression. Our
292 results establish a multilayered view of 3D genome organization in *Z. tritici*, revealing chromatin
293 conformation as a key component of genome function.

294 The core-accessory genome compartmentalization of *Z. tritici* extends beyond linear genome
295 characteristics and is mirrored in the three-dimensional organization of the nucleus. Within this nuclear
296 context, accessory chromosomes are preferentially associated with the pericentromeric regions of core
297 chromosomes while remaining excluded from interactions with core chromosome arms. Interestingly, the
298 accessory chromosomes harboring the weakest interactions with core chromosomes, specifically their

299 pericentromeric regions, were also the ones most frequently lost following treatment with carbendazim,
300 a fungicide that disrupts β-tubulin polymerization and impairs mitotic spindle assembly[28,41]. This
301 observation suggests that robust pericentromeric tethering may play a stabilizing role for accessory
302 chromosomes during mitosis. Similar phenomena have been observed in *S. cerevisiae*, where
303 microtubule-disrupting agents reduce centromere clustering, implying that centromeres are bundled at
304 the spindle pole body during interphase[42,43]. These parallels suggest that centromeric architecture in *Z.*
305 *tritici* may serve a comparable stabilizing function. Further supporting this hypothesis, accessory
306 chromosomes with stronger pericentromeric associations, such as chromosome 19, exhibited greater
307 stability under carbendazim treatment[28]. This chromosome also shows high prevalence in natural
308 populations of *Z. tritici*[27], aligning spatial stability with evolutionary persistence. In contrast, despite the
309 general presence/absence polymorphism trend among accessory chromosomes, those most frequently
310 lost under experimental conditions were not necessarily the least prevalent in global populations[27,34]. One
311 possible explanation for this discrepancy is that the strength of core-accessory chromosome interactions
312 may be strain-specific. It is likely that in different natural strains of *Z. tritici*, the core-accessory interactions
313 may vary, affecting the stability and presence of accessory chromosomes in a context-dependent manner.
314 Additionally, evolutionary pressures and local adaptation may influence the retention or loss of these
315 chromosomes, contributing to the observed diversity in the presence of accessory chromosomes across
316 strains [28]. Further research, including multiple-strain Hi-C analyses, could provide insights into how core-
317 accessory chromosome interactions have shaped the genomic architecture of *Z. tritici*.

318 In addition to the global Rabl-like organization of *Z. tritici*, we identified distinct intrachromosomal
319 compartmentalization by the presence of B compartments enriched in retrotransposons and constitutive
320 heterochromatin marks. These B compartments exhibit strong homotypic interactions, forming a spatially

321 distinct subnetwork largely insulated from the euchromatic A compartments, showing minimal inter-
322 compartment connectivity. Unlike the well-defined A/B compartmentalization observed in the human
323 genome[3] or the checkerboard interaction patterns reported in *R. irregularis*[19], *Z. tritici* displays a genome
324 topology that is dominated by internal B–B interactions. Compartmentalization inferred through principal
325 component analysis of Hi-C contact matrices revealed that B compartments are small (~60 kb), with a
326 similar size and positioning of TADs identified in our study. Specifically, these B compartments co-localize
327 with highly insulated TADs that form an interlinked network of heterochromatic regions. This suggests
328 that *Z. tritici* chromatin exhibit a heterochromatin-driven architecture, where B compartments and highly
329 insulated TADs act as spatial reservoirs for transcriptionally repressed, TE-rich genomic regions. This
330 compartmentalization likely reinforces silencing by sequestering these regions away from the
331 transcriptionally active A compartments. Such an arrangement parallels chromatin architectures observed
332 in other fungi[19,21,39]. For example, in *N. crassa*, heterochromatic domains marked by H3K9me3 aggregate
333 into discrete chromatin regions that contribute to genome stability[22,44]. In *Z. tritici*, the co-occurrence of
334 small B compartments with TAD-like structures supports a fine-scale, heterochromatin-driven genome
335 topology that enables both regulatory insulation and structural organization.

336 We identified self-interacting TAD-like domains with specific epigenetic characterization of their
337 boundaries, supporting the presence of chromatin-interacting domains as a universal genomic feature[45].
338 *Z. tritici* displays TAD-like domains of ~70 kb in size, similar to the average TAD size described in other
339 fungi[21,39], but far smaller than metazoan TADs, which typically span over megabases[45]. The detection of
340 TAD-like structures in *Z. tritici* was further supported by analysis of contact probability decay slopes
341 consistent with expectations from polymer physics modeling. These patterns, showing elevated
342 interaction frequencies at sub-100 kb distances, are consistent with the presence of interaction domains[4].

343 Unlike TADs described in metazoans, we counted only a subset of co-regulated TADs, suggesting that
344 structural features of the genome coordinate local transcriptional regulation during host-pathogen
345 interactions, similar to other plant-associated fungi[21,39]. In metazoans, the concept of TADs is also strongly
346 linked to the active loop extrusion creation process, which is dependent on cohesin and the boundary-
347 associated protein CTCF, or other insulator proteins [46]. However, self-interacting domains across the tree
348 of life were described in the absence of insulator proteins, as well as cohesin[47,48]. For instance,
349 chromosomal interaction domains (CIDs) in prokaryotes structure the genome at the gene operon level,
350 with insulated boundaries associated with highly expressed genes[49–51]. In *Z. tritici*, TAD boundaries are
351 gene-dense, TE-poor, and enriched in facultative heterochromatin histone modifications, consistent with
352 boundaries described in *V. dahliae*[21]. In *N. crassa*, interspersed heterochromatin blocks have been
353 proposed to act as domain boundaries in place of insulator proteins[18,22]. However, our findings in *Z. tritici*
354 suggest a more nuanced organization, as we observed multiple TADs between heterochromatic blocks,
355 with well-defined boundaries marked by distinct epigenetic profiles that are similar to those in *V.*
356 *dahliae*[21]. Furthermore, we observed a significant enrichment of zinc finger transcription factor DNA-
357 binding motifs at *Z. tritici* domain boundaries, notably those associated with the vertebrate insulator
358 protein ZNF263[52]. In *V. dahliae*, boundary-enriched GAAG-motifs and TATA-motifs associate with a
359 decrease in chromatin accessibility[21]. Interestingly, the *Z. tritici* IPO323 genome contains a single
360 annotated gene (ZtIPO323_082310) that shares a similar domain architecture to ZNF263, suggesting that
361 insulator-like proteins may contribute to domain boundary formation in fungi.

362 Globally, TAD-like structures exhibit low insulation scores in *Z. tritici*, consistent with previous
363 observations in other fungi[21]. However, we identified a subset of highly insulated domains (HI-TADs) that
364 coincide with TE-rich, heterochromatic regions. Similar patterns have been described in *V. dahliae* and

365 *Epichloë festucae*, where accessory genomic regions (AGRs) form structurally distinct and functionally
366 specialized chromatin domains with stronger local interactions compared to surrounding regions[21,39]. In
367 *Z. tritici*, these HI-TADs also engage more frequently in strong interactions with one another compared to
368 R-TADs, which seems reminiscent of the spatial network formed by the "TAD cliques" observed in the
369 human genome, where clusters of heterochromatic domains co-localize in 3D space[53]. Comparable
370 chromatin bundling mechanisms have also been described in *C. elegans*, where H3K9me3 promotes
371 chromosome compaction via HP1-mediated heterochromatin interactions[54]. In *N. crassa*, interspersed
372 heterochromatin blocks are described to function as boundaries, structuring TAD-like domains. Targeted
373 removal of a heterochromatic block induces localized architectural changes with minimal effects on
374 fitness[44]. The heterochromatin interaction network in *Z. tritici* shares conceptual similarities with the
375 KNOT Engaged Elements (KNOTs) described in *Arabidopsis thaliana*[55]. KNOTs are heterochromatic islands
376 within euchromatin that interact both within and between chromosomes. Notably, TEs preferentially
377 insert into these regions, and under heat stress, KNOT-associated TEs are derepressed, demonstrating
378 that these structures are dynamic and functional in TE regulation[56]. Previous studies in *Z. tritici* have
379 shown that wheat infection is accompanied by a global activation of TEs and epigenetic changes[36]. We
380 found that HI-TADs are enriched for effector genes, and some of these TADs are co-regulated *in planta,*
381 suggesting potential derepression of HI-TADs during infection. Although the mechanisms and dynamics of
382 chromatin folding during host colonization remain largely uncharacterized in fungi, the presence of
383 specialized 3D genome organization represents an evolutionary strategy to compartmentalize potentially
384 disruptive genomic elements while preserving their accessibility for regulated expression under specific
385 developmental or stress-related conditions.

386 # CONCLUSION

387 The fundamental principles of genome folding, such as compartmentalization and domain organization,
388 are broadly conserved across eukaryotes, even if the canonical definitions developed in metazoan systems
389 do not always apply uniformly across the tree of life[45]. In the fungus *Z. tritici*, we uncovered a complex,
390 multilayered chromatin architecture characterized by centromere clustering, spatial segregation between
391 core and accessory chromosomes, a long-range heterochromatin network, and TAD-like domain
392 structures. Together, these features likely contribute to this species' remarkable genome plasticity,
393 facilitating regulatory flexibility, adaptive potential, and pathogenicity. By generating a high-resolution
394 map of *Z. tritici*'s 3D genome, we lay the groundwork for mechanistic investigations into how chromatin
395 structure governs gene expression, transposable element dynamics, and genome evolution in filamentous
396 fungi. More broadly, this work advances the emerging field of comparative 3D genomics in non-model
397 species, opening new avenues for exploring genome architecture as a driver of fungal adaptation and
398 plant-pathogen interactions.

399 # METHODS

400 **Sample preparation and Hi-C sequencing**

401 The reference strain *Z. tritici* IPO323[25] was preserved in 50% glycerol at -80°C. Pre-cultures were prepared
402 with inoculations of ~100uL of glycerol stock spore suspension onto solid YMS medium (4 g/L yeast
403 extract, 4 g/L malt extract, 4 g/L sucrose, and 12 g/L of agar) and grown for 4 days at 18°C. Spores were
404 scraped from plates and re-suspended into PBS buffer (8g/L NaCl, 1.44g/L Na_2HPO_4, 0.2g/L KCl, 0.24g/L
405 KH_2PO_4) for sample preparation for epigenomics sequencing as described in Möller et al. 2023[31]. Spores
406 were fixed with formaldehyde according to PhaseGenomics instructions (Seattle, Washington, USA). Hi-C

407 experiments were performed with the Phase Genomics Proximo Hi-C Kit (Fungal), which combines four
408 restriction enzymes to ensure homogeneous digestion at AT-rich genomic regions. The resulting libraries
409 were sequenced at Biomarker Technologies GmbH (BMKgene, Münster, Germany). The sequencing was
410 performed with Illumina NovaSeq X, paired-end 150bp reads. Sample preparation, Hi-C experiment, and
411 sequencing were performed for two independent replicates.

412 **Hi-C data processing, binning, and visualization**

413 Each Hi-C read-pairs was filtered and trimmed using Trimmomatic v0.39[57] with the following settings
414 ILLUMINACLIP:${adapters}:2:30:10 LEADING:15 TRAILING:15 SLIDINGWINDOW:5:15 MINLEN:50. We
415 used HiCUP-0.9.2[58] to evaluate the quality of each Hi-C dataset. Reads were mapped against the reference
416 genome assembly of *Z. tritici* IPO323[25] using bwa-mem2[59]. The construction and analysis of Hi-C
417 interaction matrices were performed using the HiCExplorer suite of tools[60]. Each replicate interaction
418 matrix was created using *hicBuildMatrix*, by aligning the paired reads to the reference genome digested
419 *in silico* with the four restriction enzymes DpnII (GATC), DdeI (CTNAG), HinfI (GANTC), and MseI (TTAA).
420 Contact matrices were individually corrected using the iterative correction and eigenvector
421 decomposition (ICE) method via the *hicCorrectMatrix* function. The corrected contact matrices from the
422 two biological replicates were combined to generate Hi-C matrices at 1 kb, 3 kb, 10 kb, and 50 kb. The Hi-
423 C contact maps were generated with *hicPlotMatrix*. The most significant pairwise interactions were
424 extracted by filtering the observed-over-expected values above 3.5 for inter- and 1.75 for intra-
425 chromosomal interactions. The interaction link plots were generated using Circos-0.69[61]. The HiCExplorer
426 .h5 contact matrix files were converted into .cool format with *hicConvertFormat* for compatibility with the
427 *cooltools* and *cooler* packages for visualization[62]. All scripts for the analyses and visualization are available
428 at https://github.com/lorraincecile/Hi-C_Ztritici_IPO323 and 10.5281/zenodo.15395556.

429 **Estimation of chromatin folding patterns with contact probability decay**

430 To characterize chromatin folding behavior, we computed the decay of contact frequency as a function of
431 genomic distance, a method grounded in polymer physics models of chromosome organization[4]. These
432 models typically distinguish between different chromatin configurations based on the decay exponent (α)
433 of the contact probability P(s), where *s* represents genomic separation. Contact decay slopes provide
434 insights into the folding state: an exponent of ~1.5 corresponds to an equilibrium globule, indicative of
435 tightly knotted, inaccessible chromatin; values between 1 and 2 reflect a fractal globule, a compact yet
436 unknotted state; and exponents < 1 are characteristic of a tension globule, normally associated with finer
437 scale self-interacting domain units[63]. We used the *cooltools.expected_cis*[62] function to compute the
438 average contact probability, P(s), separately for core and accessory chromosomes. Genomic distances and
439 P(s) values were transformed to log10 scales, and a linear regression was fitted to the resulting log–log
440 data to estimate the decay exponent (α), which serves as a proxy for the underlying chromatin folding
441 state.

442 **Statistical Analysis of Chromosome Loss and Interaction Strength**

443 To investigate the relationship between chromosome loss and interaction strength in *Z. tritici* IPO323, we
444 extracted the average number of core-accessory chromosome strong interactions (observed vs. expected
445 > 3.5), normalized by the size of the corresponding accessory chromosome. This normalization yielded the
446 interaction strength per accessory chromosome. We compared this measure to the frequency of
447 accessory chromosome loss following beta-tubulin inhibition, described in Habig et al. (2017)[28]. A log-
448 transformed Poisson regression model was used to assess the impact of normalized interaction strength
449 on accessory chromosome loss. The model was fitted using the glm function in R (version 4.4.1), with
450 chromosome loss modeled as a Poisson-distributed response variable. The coefficients were tested for
451 statistical significance using z-tests, with p-values calculated for both the intercept and the normalized

452 interaction strength variable. Model diagnostics, including overdispersion testing using the *dispersiontest*
453 function from the AER package[64], confirmed that the Poisson distribution was an appropriate fit. The fitted
454 model was then used to predict chromosome loss, and the observed versus predicted values were
455 visualized with ggplot2[65].

456 **A/B compartmentalization analysis**

457 Compartmentalization analysis used the matrix at 3 and 10 kb resolution with functions from the cooltools
458 package[62]. We calculated PCA eigenvectors for intra- and inter-chromosomal contacts as *expected_cis* and
459 *expected_trans,* respectively. GC content was used as a phasing track to orient the eigenvector values.
460 The first three eigenvector values were manually checked, and the first eigenvector was determined to
461 have the best compatibility with the interaction pattern of the contact maps. We used the 2.5% and 97.5%
462 percentile eigenvector values as the minimum and maximum range to calculate the compartmentalization
463 strength. The compartmentalization plot was generated using the *saddleplot* function[62].

464 **Topology-associated domains (TAD) calling**

465 We established 3 kb as the smallest bin size at which at least 1000 reads covered 80% of bins for each
466 chromosome[66], and therefore the smallest scale at which we can reliably call TAD-like structures
467 (Supplementary Table S2). TAD predictions were then generated using *hicFindTADs* for HiCExplorer[60] with
468 default parameters using the contact matrix at 3kb bin size. This function calculates the insulation score
469 by evaluating interaction frequencies between adjacent bins. TAD boundaries were identified at
470 significant local minima in physical interactions, where large differences between adjacent bins yield
471 negative insulation scores, indicating “strong" insulation[60]. TADs were classified into “regular” (R-TADs)
472 and “high insulation” (HI-TADs) TADs by calculating the difference between each TAD’s maximum
473 insulation score and the minimum insulation scores of its adjacent TADs. TADs with a score difference

474 within the 20th quantile, insulation scores above the median, and flanked by two neighboring TADs with
475 negative insulation scores were considered HI-TADs.
476

477 **Analysis of genomic features**

478 Gene annotations with associated GO terms, PFAM and effector predictions were sourced from Lapalu et
479 al. (2023)[67] and accessible here (https://bioinfo.bioger.inrae.fr/portal/genome-portal/12/). Centromere
480 detections and annotations were sourced from Schotanus et al. (2015)[29]. Core genes were identified as
481 described in Minana-Posada et al. (2024)[68] as shared across 19 *Z. tritici* strains[37]. GO term enrichment
482 analysis was performed using *topGO*'s *runGOEnrichment* function[69]. GO terms with no gene associations
483 in the query lists or supported by only a single gene across the genome were excluded. False discovery
484 rate (FDR) correction was applied to all *p*-values. Enrichment analyses of effectors, core genes, and PFAM
485 domains within gene sets were performed using Fisher's exact tests, with FDR correction applied to *p*-
486 values. TE annotations were obtained from the manually curated library of Baril and Croll (2023)[70]. TAD
487 boundary motif identification and enrichment were performed with XSTREME with default parameters
488 and compared to JASPAR database motifs[71] using Tomtom from the MEME suite tools[72]. We used the RIP
489 composite index to identify RIP-like signatures in 1 kb sliding windows across the genome as described in
490 Lorrain et al. (2021)[35]. A positive RIP composite index value reflects the presence of RIP-like mutations.
491 The distribution of genes, TEs and RIP-like signatures across TADs and their boundaries was analyzed using
492 the EnrichedHeatmap package in R[73].

493 **Gene and TE expression analyses**

494 RNA-seq data for *Z. tritici* IPO323 during *in planta* infection, comprising four distinct infection stages, was
495 obtained from Haueisen et al. (2018)[74], while *in vitro* RNA-seq data was sourced from Möller et al.
496 (2023)[31]. After trimming low-quality reads, the resulting high-quality reads were aligned to the IPO323

497 reference genome using STAR[75], with parameters configured to allow the inclusion of multimapping reads.
498 To capture the expression of genes and TEs, multimapper reads were reassigned using TEtranscript[76],
499 which ensures precise allocation of reads to the transcript sequences[67]
500 (https://bioinfo.bioger.inrae.fr/portal/genome-portal/12/) and TE library of *Z. tritici* IPO323[70]. Differential
501 expression analysis was performed using DESeq2[77], comparing expression levels across the biotrophic
502 phases (stages A and B), necrotrophic phases (stages C and D)[74], and *in vitro* growth conditions.

503 **Characterization of epigenetic profiles**

504 Histone modifications, centromere detection, and cytosine DNA methylation (5mC) level enrichments
505 across the *Z. tritici* IPO323 genome were assessed using publicly available chromatin immunoprecipitation
506 followed by sequencing (ChIP-seq) and whole-genome bisulfite sequencing (WGBS) datasets. ChIP-seq
507 datasets for CenH3 and H3K9me2 were obtained from Schotanus et al. (2015)[29], while datasets for
508 H3K36me3, H4K20me3, H4K20me1, H3K27me3, H3K27me2, and H3K4me2 were sourced from Möller et
509 al. (2023)[31]. Reads were preprocessed using Trimmomatic v0.39[57], with parameters
510 ILLUMINACLIP:${adapters}:2:30:10 LEADING:3 TRAILING:3 SLIDINGWINDOW:4:15 MINLEN:30 and
511 ILLUMINACLIP:${adapters}:2:30:10:2:keepBothReads HEADCROP:5 LEADING:3 TRAILING:3
512 SLIDINGWINDOW:4:15 MINLEN:30 for the single and paired end samples respectively. The filtered reads
513 were mapped to the IPO323 reference genome using Bowtie2 with default settings[78]. To account for the
514 repetitive nature of TEs in the genome, multimapping reads were subsequently mapped using Allo[79], an
515 approach tailored to improve mapping accuracy in repeat-rich regions. Reads with a mapping quality score
516 below 30 and PCR duplicates identified by Picard v2.26.2[80] were excluded from further analysis. To
517 visualize enrichment levels across the genome, histone enrichment profiles were generated as bigWig and
518 bedGraph files in bins of 10 bp, 3 kb, and 10 kb.

519 Bisulfite sequencing data was retrieved from Möller et al. (2021)[32] for cytosine DNA methylation analysis.
520 Cultures were inoculated directly from glycerol stocks into liquid YMS medium and grown for 5 days. The
521 Illumina HiSeq3000 paired-end raw reads were filtered using Trimmomatic[57] parameters HEADCROP:10
522 CROP:140 LEADING:3 TRAILING:3 SLIDINGWINDOW:4:15 MINLEN:50 and subsequently mapped and
523 deduplicated using Bismark[81]. The methylated sites in all contexts (CG, CHG, CHH) were extracted using
524 the function *bismark_methylation_extractor,* and filtered to remove sites not supported by at least four
525 reads and more than 50% of the mapped reads. The weighted methylation average was calculated for 10
526 bp, 3 kb and 10 kb windows. The distribution of histone marks and 5mC levels across TADs and their
527 boundaries was analyzed using the EnrichedHeatmap package in R[73].

528 **TAD co-expression analysis**

529 To investigate the co-regulation of genes and TEs within TADs, we constructed a linear model in Python
530 as described in Winter et al. (2018)[39]. The model utilized the log2-fold change in gene expression between
531 *in planta* and *in vitro* stages as the response variable, with TAD membership as the main predictor. We
532 developed nested models by incorporating additional genomic features known to affect gene expression,
533 including GC content and distance to the nearest TE. The nested models' performance was evaluated
534 using the Akaike Information Criterion (AIC) and likelihood ratio tests. We defined TADs as co-regulated
535 TADs with more than 10 co-expressed genes and TEs.

536 Code availability

537 All custom scripts generated for data analyses and visualization are available at
538 https://github.com/lorraincecile/Hi-C_Ztritici_IPO323. The Hi-C contact matrices and TAD annotations as
539 well as source data for figures and tables presented in this study are available at
540 10.5281/zenodo.15395556.

541 ## Data availability

542 The Hi-C sequencing data is publicly available from the NCBI Gene Expression Omnibus (GEO) under the
543 accession GSE296663. *In planta*[74] and *in vitro*[31] RNA-seq datasets are available at the GEO accession
544 number GSE106136 and the accession number NCBI BioProjects PRJNA902413, respectively. The ChIP-seq
545 datasets for CenH3 and H3K9me2[29] are accessible through the SRA ID SRP059394. The ChIP-seq datasets
546 for H3K36me3, H4K20me3, H4K20me1, H3K27me3, H3K27me2, and H3K4me2[31] are available at the SRA
547 ID SRP411885. Whole-genome bisulfite sequencing[32] data are available at SRA under BioProject ID
548 PRJNA614493.

549 ## Acknowledgments

550 Ivona Glavincheska and Cecile Lorrain are funded by a SNSF Ambizione grant (PZ00P3_209022). We thank
551 Prof. Bruce McDonald and ETH Zurich for funding the Hi-C sequencing.

552 ## Authors contributions

553 IG and CL designed the experiments. IG performed data acquisition. IG and CL performed the data analysis
554 and interpretation. CL conceptualized the study. IG and CL wrote and revised the manuscript.

555 ## REFERENCES

556 1. Sexton, T. & Cavalli, G. The Role of Chromosome Domains in Shaping the Functional
557 Genome. *Cell* **160**, 1049–1059 (2015).
558 2. Hoencamp, C. *et al.* 3D genomics across the tree of life reveals condensin II as a
559 determinant of architecture type. *Science* **372**, 984–989 (2021).
560 3. Lieberman-Aiden, E. *et al.* Comprehensive Mapping of Long-Range Interactions Reveals
561 Folding Principles of the Human Genome. *Science* **326**, 289–293 (2009).

562 4. Esposito, A. *et al.* Polymer physics reveals a combinatorial code linking 3D chromatin
563 architecture to 1D chromatin states. *Cell Reports* **38**, 110601 (2022).
564 5. Szalay, M.-F., Majchrzycka, B., Jerković, I., Cavalli, G. & Ibrahim, D. M. Evolution and
565 function of chromatin domains across the tree of life. *Nat Struct Mol Biol* **31**, 1824–1837
566 (2024).
567 6. Cremer, T. *et al.* Rabl's model of the interphase chromosome arrangement tested in Chinise
568 hamster cells by premature chromosome condensation and laser-UV-microbeam
569 experiments. *Hum Genet* **60**, 46–56 (1982).
570 7. Álvarez-González, L. *et al.* Principles of 3D chromosome folding and evolutionary genome
571 reshuffling in mammals. *Cell Reports* **41**, 111839 (2022).
572 8. Dixon, J. R. *et al.* Topological Domains in Mammalian Genomes Identified by Analysis of
573 Chromatin Interactions. *Nature* **485**, 376 (2012).
574 9. Long, H. S. *et al.* Making sense of the linear genome, gene function and TADs. *Epigenetics*
575 *& Chromatin* **15**, 4 (2022).
576 10. Flavahan, W. A. *et al.* Insulator dysfunction and oncogene activation in IDH mutant gliomas.
577 *Nature* **529**, 110–114 (2016).
578 11. Valton, A.-L. & Dekker, J. TAD disruption as oncogenic driver. *Current Opinion in Genetics*
579 *& Development* **36**, 34–40 (2016).
580 12. Dong, P. *et al.* 3D Chromatin Architecture of Large Plant Genomes Determined by Local
581 A/B Compartments. *Mol Plant* **10**, 1497–1509 (2017).
582 13. Li, E. *et al.* Long-range interactions between proximal and distal regulatory regions in maize.
583 *Nat Commun* **10**, 2633 (2019).
584 14. Ricci, W. A. *et al.* Widespread long-range cis-regulatory elements in the maize genome. *Nat*
585 *Plants* **5**, 1237–1249 (2019).

586 15. Dong, P., Tu, X., Liang, Z., Kang, B.-H. & Zhong, S. Plant and animal chromatin three-
587 dimensional organization: similar structures but different functions. *J Exp Bot* **71**, 5119–
588 5128 (2020).
589 16. Case, N. T. *et al.* Fungal impacts on Earth's ecosystems. *Nature* **638**, 49–57 (2025).
590 17. Belton, J.-M. *et al.* Hi-C: A comprehensive technique to capture the conformation of
591 genomes. *Methods* **58**, 10.1016/j.ymeth.2012.05.001 (2012).
592 18. Torres, D. E., Reckard, A. T., Klocko, A. D. & Seidl, M. F. Nuclear genome organization in
593 fungi: from gene folding to Rabl chromosomes. *FEMS Microbiology Reviews* **47**, fuad021
594 (2023).
595 19. Yildirir, G. *et al.* Long reads and Hi-C sequencing illuminate the two-compartment genome
596 of the model arbuscular mycorrhizal symbiont Rhizophagus irregularis. *New Phytologist*
597 **233**, 1097–1107 (2022).
598 20. Schalbetter, S. A., Fudenberg, G., Baxter, J., Pollard, K. S. & Neale, M. J. Principles of
599 meiotic chromosome assembly revealed in S. cerevisiae. *Nat Commun* **10**, 4795 (2019).
600 21. Torres, D. E. *et al.* Implications of the three-dimensional chromatin organization for genome
601 evolution in a fungal plant pathogen. *Nat Commun* **15**, 1701 (2024).
602 22. Galazka, J. M. *et al.* Neurospora chromosomes are organized by blocks of importin alpha-
603 dependent heterochromatin that are largely independent of H3K9me3. *Genome Res.* **26**,
604 1069–1080 (2016).
605 23. Rodriguez, S. *et al.* The genome organization of Neurospora crassa at high resolution
606 uncovers principles of fungal chromosome topology. *G3 Genes|Genomes|Genetics* **12**,
607 jkac053 (2022).
608 24. Stukenbrock, E. H., Banke, S., Javan-Nikkhah, M. & McDonald, B. A. Origin and
609 Domestication of the Fungal Wheat Pathogen Mycosphaerella graminicola via Sympatric
610 Speciation. *Molecular Biology and Evolution* **24**, 398–411 (2007).

611 25. Goodwin, S. B. *et al.* Finished Genome of the Fungal Wheat Pathogen Mycosphaerella
612 graminicola Reveals Dispensome Structure, Chromosome Plasticity, and Stealth
613 Pathogenesis. *PLOS Genetics* **7**, e1002070 (2011).
614 26. Feurtey, A. *et al.* Genome compartmentalization predates species divergence in the plant
615 pathogen genus Zymoseptoria. *BMC Genomics* **21**, 588 (2020).
616 27. Feurtey, A. *et al.* A thousand-genome panel retraces the global spread and adaptation of a
617 major fungal crop pathogen. *Nat Commun* **14**, 1059 (2023).
618 28. Habig, M., Quade, J. & Stukenbrock, E. H. Forward Genetics Approach Reveals Host
619 Genotype-Dependent Importance of Accessory Chromosomes in the Fungal Wheat
620 Pathogen Zymoseptoria tritici. *mBio* **8**, e01919-17 (2017).
621 29. Schotanus, K. *et al.* Histone modifications rather than the novel regional centromeres of
622 Zymoseptoria tritici distinguish core and accessory chromosomes. *Epigenetics & Chromatin*
623 **8**, 41 (2015).
624 30. Habig, M., Lorrain, C., Feurtey, A., Komluski, J. & Stukenbrock, E. H. Epigenetic
625 modifications affect the rate of spontaneous mutations in a pathogenic fungus. *Nat Commun*
626 **12**, 5869 (2021).
627 31. Möller, M., Ridenour, J. B., Wright, D. F., Martin, F. A. & Freitag, M. H4K20me3 is important
628 for Ash1-mediated H3K36me3 and transcriptional silencing in facultative heterochromatin in
629 a fungal pathogen. *PLoS Genet* **19**, e1010945 (2023).
630 32. Möller, M. *et al.* Recent loss of the Dim2 DNA methyltransferase decreases mutation rate in
631 repeats and changes evolutionary trajectory in a fungal pathogen. *PLOS Genetics* **17**,
632 e1009448 (2021).
633 33. Möller, M. *et al.* Destabilization of chromosome structure by histone H3 lysine 27
634 methylation. *PLOS Genetics* **15**, e1008093 (2019).

635 34. Möller, M., Habig, M., Freitag, M. & Stukenbrock, E. H. Extraordinary Genome Instability
636 and Widespread Chromosome Rearrangements During Vegetative Growth. *Genetics* **210**,
637 517–529 (2018).
638 35. Lorrain, C., Feurtey, A., Möller, M., Haueisen, J. & Stukenbrock, E. Dynamics of
639 transposable elements in recently diverged fungal pathogens: lineage-specific transposable
640 element content and efficiency of genome defenses. *G3 Genes|Genomes|Genetics* **11**,
641 jkab068 (2021).
642 36. Meile, L. *et al.* Chromatin Dynamics Contribute to the Spatiotemporal Expression Pattern of
643 Virulence Genes in a Fungal Plant Pathogen. *mBio* **11**, 10.1128/mbio.02343-20 (2020).
644 37. Badet, T., Oggenfuss, U., Abraham, L., McDonald, B. A. & Croll, D. A 19-isolate reference-
645 quality global pangenome for the fungal wheat pathogen Zymoseptoria tritici. *BMC Biol* **18**,
646 12 (2020).
647 38. Ortabozkoyun, H. *et al.* Members of an array of zinc-finger proteins specify distinct *Hox*
648 chromatin boundaries. *Molecular Cell* **84**, 3406-3422.e6 (2024).
649 39. Winter, D. J. *et al.* Repeat elements organise 3D genome structure and mediate
650 transcription in the filamentous fungus Epichloë festucae. *PLoS Genet* **14**, e1007467
651 (2018).
652 40. Shao, W. *et al.* The jet-like chromatin structure defines active secondary metabolism in
653 fungi. *Nucleic Acids Research* **52**, 4906–4921 (2024).
654 41. Davidse, L. C. & Flach, W. Differential binding of methyl benzimidazol-2-yl carbamate to
655 fungal tubulin as a mechanism of resistance to this antimitotic agent in mutant strains of
656 Aspergillus nidulans. *J Cell Biol* **72**, 174–193 (1977).
657 42. Goto, B., Okazaki, K. & Niwa, O. Cytoplasmic microtubular system implicated in de novo
658 formation of a Rabl-like orientation of chromosomes in fission yeast. *J Cell Sci* **114**, 2427–
659 2435 (2001).

660 43. Jin, Q. W., Fuchs, J. & Loidl, J. Centromere clustering is a major determinant of yeast
661 interphase nuclear organization. *J Cell Sci* **113 (Pt 11)**, 1903–1912 (2000).
662 44. Reckard, A. T. *et al.* A Constitutive Heterochromatic Region Shapes Genome Organization
663 and Impacts Gene Expression in Neurospora crassa. *bioRxiv* 2024.06.07.597955 (2024)
664 doi:10.1101/2024.06.07.597955.
665 45. Szalay, M.-F., Majchrzycka, B., Jerković, I., Cavalli, G. & Ibrahim, D. M. Evolution and
666 function of chromatin domains across the tree of life. *Nat Struct Mol Biol* 1–14 (2024)
667 doi:10.1038/s41594-024-01427-y.
668 46. Davidson, I. F. *et al.* CTCF is a DNA-tension-dependent barrier to cohesin-mediated loop
669 extrusion. *Nature* **616**, 822–827 (2023).
670 47. Oberbeckmann, E., Quililan, K., Cramer, P. & Oudelaar, A. M. In vitro reconstitution of
671 chromatin domains shows a role for nucleosome positioning in 3D genome organization.
672 *Nat Genet* **56**, 483–492 (2024).
673 48. Wing Shun Li *et al.* Mature chromatin packing domains persist after RAD21 depletion in 3D.
674 *Science Advances* (2025) doi:10.1126/sciadv.adp0855.
675 49. Trussart, M. *et al.* Defined chromosome structure in the genome-reduced bacterium
676 Mycoplasma pneumoniae. *Nat Commun* **8**, 14665 (2017).
677 50. Le, T. B. K., Imakaev, M. V., Mirny, L. A. & Laub, M. T. High-resolution mapping of the
678 spatial organization of a bacterial chromosome. *Science* **342**, 731–734 (2013).
679 51. Marbouty, M. *et al.* Metagenomic chromosome conformation capture (meta3C) unveils the
680 diversity of chromosome organization in microorganisms. *Elife* **3**, e03318 (2014).
681 52. Ortabozkoyun, H. *et al.* Members of an array of zinc-finger proteins specify distinct *Hox*
682 chromatin boundaries. *Molecular Cell* **84**, 3406-3422.e6 (2024).
683 53. Liyakat Ali, T. M., Brunet, A., Collas, P. & Paulsen, J. TAD cliques predict key features of
684 chromatin organization. *BMC Genomics* **22**, 499 (2021).

685 54. Qian Bian *et al.* Histone H3K9 methylation promotes formation of genome compartments in
686 Caenorhabditis elegans via chromosome compaction and perinuclear anchoring.
687 *Proceedings of the National Academy of Sciences of the United States of America* **117**,
688 11459–11470 (2020).
689 55. Grob, S., Schmid, M. W. & Grossniklaus, U. Hi-C Analysis in *Arabidopsis* Identifies the
690 *KNOT*, a Structure with Similarities to the *flamenco* Locus of *Drosophila*. *Molecular Cell* **55**,
691 678–693 (2014).
692 56. Sun, L. *et al.* Heat stress-induced transposon activation correlates with 3D chromatin
693 organization rearrangement in Arabidopsis. *Nat Commun* **11**, 1886 (2020).
694 57. Bolger, A. M., Lohse, M. & Usadel, B. Trimmomatic: a flexible trimmer for Illumina sequence
695 data. *Bioinformatics* **30**, 2114–2120 (2014).
696 58. Wingett, S. *et al.* HiCUP: pipeline for mapping and processing Hi-C data. *F1000Res* **4**, 1310
697 (2015).
698 59. Vasimuddin, Md., Misra, S., Li, H. & Aluru, S. Efficient Architecture-Aware Acceleration of
699 BWA-MEM for Multicore Systems. in *2019 IEEE International Parallel and Distributed*
700 *Processing Symposium (IPDPS)* 314–324 (2019). doi:10.1109/IPDPS.2019.00041.
701 60. Ramírez, F. *et al.* High-resolution TADs reveal DNA sequences underlying genome
702 organization in flies. *Nature Communications* **9**, 189 (2018).
703 61. Krzywinski, M. I. *et al.* Circos: An information aesthetic for comparative genomics. *Genome*
704 *Res.* (2009) doi:10.1101/gr.092759.109.
705 62. Open2C *et al.* Cooltools: Enabling high-resolution Hi-C analysis in Python. *PLOS*
706 *Computational Biology* **20**, e1012067 (2024).
707 63. Sanborn, A. L. *et al.* Chromatin extrusion explains key features of loop and domain
708 formation in wild-type and engineered genomes. *Proc Natl Acad Sci U S A* **112**, E6456-
709 6465 (2015).

710 64. Kleiber, C. & Zeileis, A. Diagnostics and Alternative Methods of Regression. in *Applied*
711 *Econometrics with R* (eds. Kleiber, C. & Zeileis, A.) 1–27 (Springer, New York, NY, 2008).
712 doi:10.1007/978-0-387-77318-6_4.
713 65. Wickham, H. *Ggplot2*. (Springer International Publishing, Cham, 2016). doi:10.1007/978-3-
714 319-24277-4.
715 66. Rao, S. S. P. *et al.* A 3D map of the human genome at kilobase resolution reveals principles
716 of chromatin looping. *Cell* **159**, 1665–1680 (2014).
717 67. Lapalu, N. *et al. Improved Gene Annotation of the Fungal Wheat Pathogen* Zymoseptoria
718 Tritici *Based on Combined Iso-Seq and RNA-Seq Evidence*.
719 http://biorxiv.org/lookup/doi/10.1101/2023.04.26.537486 (2023)
720 doi:10.1101/2023.04.26.537486.
721 68. Miñana-Posada, S., Lorrain, C., McDonald, B. A. & Feurtey, A. Thermal adaptation in
722 worldwide collections of a major fungal pathogen. 2024.09.12.612681 Preprint at
723 https://doi.org/10.1101/2024.09.12.612681 (2024).
724 69. topGO. *Bioconductor* http://bioconductor.org/packages/topGO/ (2024).
725 70. Baril, T. & Croll, D. A pangenome-guided manually curated library of transposable elements
726 for Zymoseptoria tritici. *BMC Research Notes* **16**, 335 (2023).
727 71. Sandelin, A., Alkema, W., Engström, P., Wasserman, W. W. & Lenhard, B. JASPAR: an
728 open-access database for eukaryotic transcription factor binding profiles. *Nucleic Acids*
729 *Research* **32**, D91–D94 (2004).
730 72. MEME Suite: tools for motif discovery and searching | Nucleic Acids Research | Oxford
731 Academic. https://academic.oup.com/nar/article/37/suppl_2/W202/1135092.
732 73. Gu, Z., Eils, R., Schlesner, M. & Ishaque, N. EnrichedHeatmap: an R/Bioconductor package
733 for comprehensive visualization of genomic signal associations. *BMC Genomics* **19**, 234
734 (2018).

735 74. Haueisen, J. *et al.* Highly flexible infection programs in a specialized wheat pathogen. *Ecol*
736 *Evol* **9**, 275–294 (2018).
737 75. Dobin, A. *et al.* STAR: ultrafast universal RNA-seq aligner. *Bioinformatics* **29**, 15–21 (2013).
738 76. Jin, Y., Tam, O. H., Paniagua, E. & Hammell, M. TEtranscripts: a package for including
739 transposable elements in differential expression analysis of RNA-seq datasets.
740 *Bioinformatics* **31**, 3593–3599 (2015).
741 77. Love, M. I., Huber, W. & Anders, S. Moderated estimation of fold change and dispersion for
742 RNA-seq data with DESeq2. *Genome Biology* **15**, 550 (2014).
743 78. Langmead, B. & Salzberg, S. L. Fast gapped-read alignment with Bowtie 2. *Nat Methods* **9**,
744 357–359 (2012).
745 79. Morrissey, A., Shi, J., James, D. Q. & Mahony, S. Accurate allocation of multimapped reads
746 enables regulatory element analysis at repeats. *Genome Res* **34**, 937–951 (2024).
747 80. Picard Tools - By Broad Institute. https://broadinstitute.github.io/picard/.
748 81. Krueger, F. & Andrews, S. R. Bismark: a flexible aligner and methylation caller for Bisulfite-
749 Seq applications. *Bioinformatics* **27**, 1571–1572 (2011).
750 82. Minana-Posada, S., Feurtey, A., Alassimone, J., McDonald, B. A. & Lorrain, C. Responses
751 to temperature shocks in Zymoseptoria tritici reveal specific transcriptional reprogramming
752 and novel candidate genes for thermal adaptation. 2024.12.16.628617 Preprint at
753 https://doi.org/10.1101/2024.12.16.628617 (2024).
754

755 # LEGENDS

756 **Fig. 1: The Rabl-like three-dimensional structure of *Zymoseptoria tritici* is compartmentalized**. a)
757 Heatmap of genome-wide normalized Hi-C contact map at 10kb resolution. Contact numbers per 10kb
758 bins are represented in a log scale. Chromosomes are represented by ideograms with purple marking the

759 centromeres[29]. b) Strongest inter-chromosomal interactions with an observed-to-expected value >3.5 at
760 10 kb bin resolution. Core chromosomes are represented in light blue. Accessory chromosomes are
761 represented in dark blue. Centromeres are marked by triangles. H3K9me3 enrichment is shown in the
762 orange histogram. Links represent inter-chromosomal pericentromere-pericentromere interactions
763 (purple), accessory-core chromosome (green), or any other interactions (grey). c) Contact probability (top)
764 and contact frequency decay slope (bottom) against genomic distance for core (green) and accessory
765 (orange) chromosomes.
766
767 **Fig. 2: Homotypic interactions and epigenomic features of A/B compartments in the *Zymoseptoria tritici***
768 **genome.** a) Saddle plot representing genome-wide intrachromosomal Hi-C interactions at 3 kb resolution.
769 Homotypic B-B interactions are represented in the top-left, while A-A interactions are observed in the
770 bottom-right. b) Enrichment of histone modifications across A and B compartments, highlighting distinct
771 chromatin states. c) Genomic composition of A and B compartments, showing proportions of genes
772 (green), transposable elements (orange), and intergenic regions (grey). d) Density of genes (green) and
773 transposable elements (orange) across A and B compartments. e) Distribution of transposable element
774 families within A and B compartments. f) *In vitro* Expression levels of genes (green) and transposable
775 elements (orange) in A and B compartments.
776
777 **Fig. 3: The genome of *Zymoseptoria tritici* forms topology-associated domain-like (TAD-like) structures**
778 **with specific genomic and epigenomic signatures.** a) Close-up of Hi-C contact map showing local
779 interaction frequencies at 3 kb bins resolution and detection of self-interacting TAD-like structures.
780 Insulation score was calculated with a genome-wide sliding window approach. Predicted TAD-like domains
781 are represented by black triangles, and boundaries are indicated by red arrows. b) Heatmap of chromatin
782 insulation scores, histone modifications (H3K36me3 and H3K9me3), gene, and TE density enrichment

783 centered on domain boundaries, with 35 kb upstream and downstream regions shown per row. The top
784 panel shows the average profile across all boundaries depicted in the heatmap. c) Close-up example of
785 TAD-like annotations on chromosome 4 of *Z. tritici* IPO323. From top to bottom: strongest intra-
786 chromosomal links (observed/expected > 1.75) across chromosome 4; chromosome 4 Hi-C contact map
787 with TAD annotated by triangles; insulation scores within chromosome 4; histone modifications for
788 euchromatin H3K4me2, heterochromatin H3K9me2, H3K9me3, and facultative heterochromatin
789 H3K27me2, H3K27me3, H3K36me3, H3K20me1, H4K20me3. d) Heatmap of chromatin insulation scores,
790 histone modifications, 5-methylcytosine DNA methylation (5mC), repeat-induced point mutation (RIP)
791 composite index frequency, genes, and TEs density centered on TAD-like domains, with 35 kb upstream
792 and downstream regions shown per row. The top panel shows the average profile across all TADs depicted
793 in the heatmap. Highly-insulated TADs (HI-TADs) are depicted by solid lines, and "regular-TADs" (R-TADs)
794 are depicted by dashed lines.
795
796 **Supplementary Fig. S1: Quality assessment of the Hi-C libraries replicates.** a) Pearson correlation
797 between Hi-C contact map replicates in *Zymoseptoria tritici* IPO323 (Pearson correlation = 0.87). b) Hi-C
798 libraries quality filtering with the HiCUP-0.9.2[58] pipeline.
799
800 **Supplementary Fig. S2: *Zymoseptoria tritici* IPO323 Hi-C contact map 10kb bins normalized per genomic**
801 **distance as observed/expected interactions.**
802
803 **Supplementary Fig. S3: Strongest interactions in *Zymoseptoria tritici* IPO323.** Links represent the
804 strongest interactions with observed-to-expected values >3.5 at 10 kb bin resolution for a) all strong
805 interactions, b) inter-chromosomal pericentromere-pericentromere interactions, c) accessory-core
806 chromosome interactions with inter-chromosomal pericentromere-pericentromere interactions (purple),

807 accessory-core chromosome (green), H3K9me3-H3K9me3 interactions (orange) or any other interactions
808 (grey), d) H3K9me3-H3K9me3 interactions.
809
810 **Supplementary Fig. S4: Relationship between chromosomal interaction strength and chromosome loss**
811 **in *Zymoseptoria tritici* strain IPO323, after carbendazim treatment**[28]. Scatterplot showing the association
812 between log-transformed normalized Hi-C interaction strength (x-axis) and the frequency of chromosome
813 loss (y-axis) across individual chromosomes. A dashed grey line indicates the predicted linear relationship.
814 The model indicates a significant inverse relationship between interaction strength and chromosome loss
815 (Poisson GLM, $p < 0.05$).
816
817 **Supplementary Fig. S5: Interchromosomal compartmentalization in *Zymoseptoria tritici* IPO323.** a) Self-
818 interacting compartments were identified from Hi-C contact matrix at 10 kb resolution. Principal
819 component analysis (PCA) of interchromosomal contact frequencies was used to extract the first
820 eigenvector (E1), with positive and negative values annotated in yellow and purple, respectively. The
821 eigenvector track is shown above each panel. The Hi-C contact map with 10 kb resolution is shown for all
822 chromosomes, shown by ideograms on the side, with centromeres represented in purple. b) Saddle plot
823 representing genome-wide Hi-C interactions at 10 kb resolution. Homotypic interactions between regions
824 associated with a negative E1 are represented in the top-left, while positive E1 region interactions are
825 observed in the bottom-right.
826
827 **Supplementary Fig. S6: Intrachromosomal A/B compartments in *Zymoseptoria tritici* IPO323.** For each
828 chromosome, A/B compartments were identified from Hi-C contact matrices at 3 kb resolution. Principal
829 component analysis (PCA) of intrachromosomal contact frequencies was used to extract the first
830 eigenvector (E1), with positive and negative values corresponding to A (yellow) and B (purple)

831 compartments, respectively. The eigenvector track is shown above each panel. Enrichment of H3K9me3
832 per 10 kb window is displayed as a histogram below the eigenvector track. Hi-C contact maps are shown
833 for individual chromosomes. Centromeres are represented by yellow stars.
834
835 **Supplementary Fig. S7: TAD-like boundaries characteristics in core and accessory chromosomes of**
836 ***Zymoseptoria tritici* IPO323.** Heatmaps of chromatin insulation scores, enrichment in histone
837 modifications (H3K4me2, H3K9me2, H3K9me3, H3K27me2, H3K27me3, H3K36me3, H4K20me1,
838 H4K20me3), 5-methylcytosine DNA methylation (5mC), repeat-induced point mutation (RIP) composite
839 index frequency, genes, and TEs density centered on domain boundaries, with 35 kb upstream and
840 downstream regions shown per row. The top panel shows the average profile across all boundaries
841 depicted in the heatmap.
842
843 **Supplementary Fig. S8: *In vitro* Expression levels of genes in topology-associated domains and**
844 **boundaries.** Genes are represented in green and transposable elements in orange. Statistical significance
845 of differences between TADs and boundaries was assessed using a two-sided Mann-Whitney U test.
846
847 **Supplementary Fig. S9: Strongest interactions between topology-associated domains (TADs).**
848 Distribution of observed-to-expected contact ratios > 1.75 from the 10 kb resolution interaction matrix,
849 highlighting the strongest intrachromosomal interactions classified as either highly insulated TADs (HI-
850 TADs) or regular TADs (R-TADs). Statistical significance of differences between groups was assessed using
851 a two-sided Mann-Whitney U test.
852
853 **Supplementary Fig. S10: *In vitro* Expression levels of genes in regular topology-associated domains (R-**
854 **TADs) and highly insulated topology-associated domains (HI-TADs).** Genes are represented in green and

855 transposable elements in orange. Statistical significance of differences between HI-TADs and R-TADs was
856 assessed using a two-sided Mann-Whitney U test.
857
858 **Supplementary Fig. S11: Co-regulated topology-associated domains (TADs) during wheat infection**
859 **stages.** Effect sizes from linear regression models quantified the contribution of each topologically
860 associating domain (TAD) to differential gene expression between in vitro growth on YMA medium and
861 various in planta infection stages (stage A: early biotrophic, stage B: late biotrophic, stage C: early
862 necrotrophic, and stage D: late necrotrophic). Each point represents the mean effect size per TAD,
863 accompanied by a 95% confidence interval. TADs with statistically significant effects (i.e., confidence
864 intervals not overlapping zero) are highlighted in color and annotated with their chromosome and TAD
865 identifiers. Values reflect normalized means derived from two independent biological replicates [74].
866
867 **Supplementary Fig. S12: Overlap between TAD categories.** Venn diagram illustrating the overlap among
868 three categories of topology-associated domains (TADs): co-regulated TADs (defined as containing ≥10
869 genes or transposable elements with coordinated expression), highly insulated TADs (HI-TADs; identified
870 by elevated insulation scores), and accessory chromosome TADs (located on accessory chromosomes).
871
872 **Supplementary Table S1: Quality assessment of Hi-C sequencing data.**
873 **Supplementary Table S2: Hi-C matrix contact coverage per chromosome.**
874 **Supplementary Table S3: Strongest interchromosomal interactions.** Hi-C interactions were normalized
875 in observed vs expected (o/e) contacts.
876 **Supplementary Table S4: Contact frequency decay exponent per chromosome.**
877 **Supplementary Table S5: A/B compartments from PCA eigenvector analysis.**
878 **Supplementary Table S6: Gene/TE content of A/B compartments.**

879 **Supplementary Table S7: TE content of A/B compartments.**

880 **Supplementary Table S8: Gene ontology enrichment in A compartment.**

881 **Supplementary Table S9: Gene ontology enrichment in B compartment.**

882 **Supplementary Table S10: Topology-associated domains (TADs) annotation in the *Z. tritici* IPO323**
883 **genome.**

884 **Supplementary Table S11: TAD boundaries annotations in the *Z. tritici* IPO323 genome.**

885 **Supplementary Table S12: TADs summary metrics in core and accessory chromosomes.**

886 **Supplementary Table S13: Core orthologous genes enrichment in TAD boundaries.** The core orthologous
887 genes are present in 19 reference genomes of *Z. tritici* [37,82].

888 **Supplementary Table S14: PFAM domains enrichment in TAD boundaries.**

889 **Supplementary Table S15: Gene ontology enrichment in TAD boundaries.**

890 **Supplementary Table S16: Motifs enrichment in TAD boundaries.**

891 **Supplementary Table S17: ZNF263 BLASTp searches in *Zymoseptoria tritici* IPO323 proteome**

892 **Supplementary Table S18: Annotation of highly insulated TADs (HI-TADs) and regular TADs (R-TADs).**

893 **Supplementary Table S19: Effector gene enrichment in highly insulated TADs (HI-TADs)**

894 **Supplementary Table S20: Gene/TE expression analysis *in planta* stage A (early biotrophic phase)**
895 **versus *in vitro*.**

896 **Supplementary Table S21: Gene/TE expression analysis *in planta* stage B (late biotrophic phase) versus**
897 ***in vitro*.**

898 **Supplementary Table S22: Gene/TE expression analysis *in planta* stage C (early necrotrophic phase)**
899 **versus *in vitro*.**

900 **Supplementary Table S23: Gene/TE expression analysis *in planta* stage D (late necrotrophic phase)**
901 **versus *in vitro*.**

902 **Supplementary Table S24: Table S23: Linear models for TAD co-expression analyses.**

903 **Supplementary Table S25: Summary metrics of co-regulated TADs.**

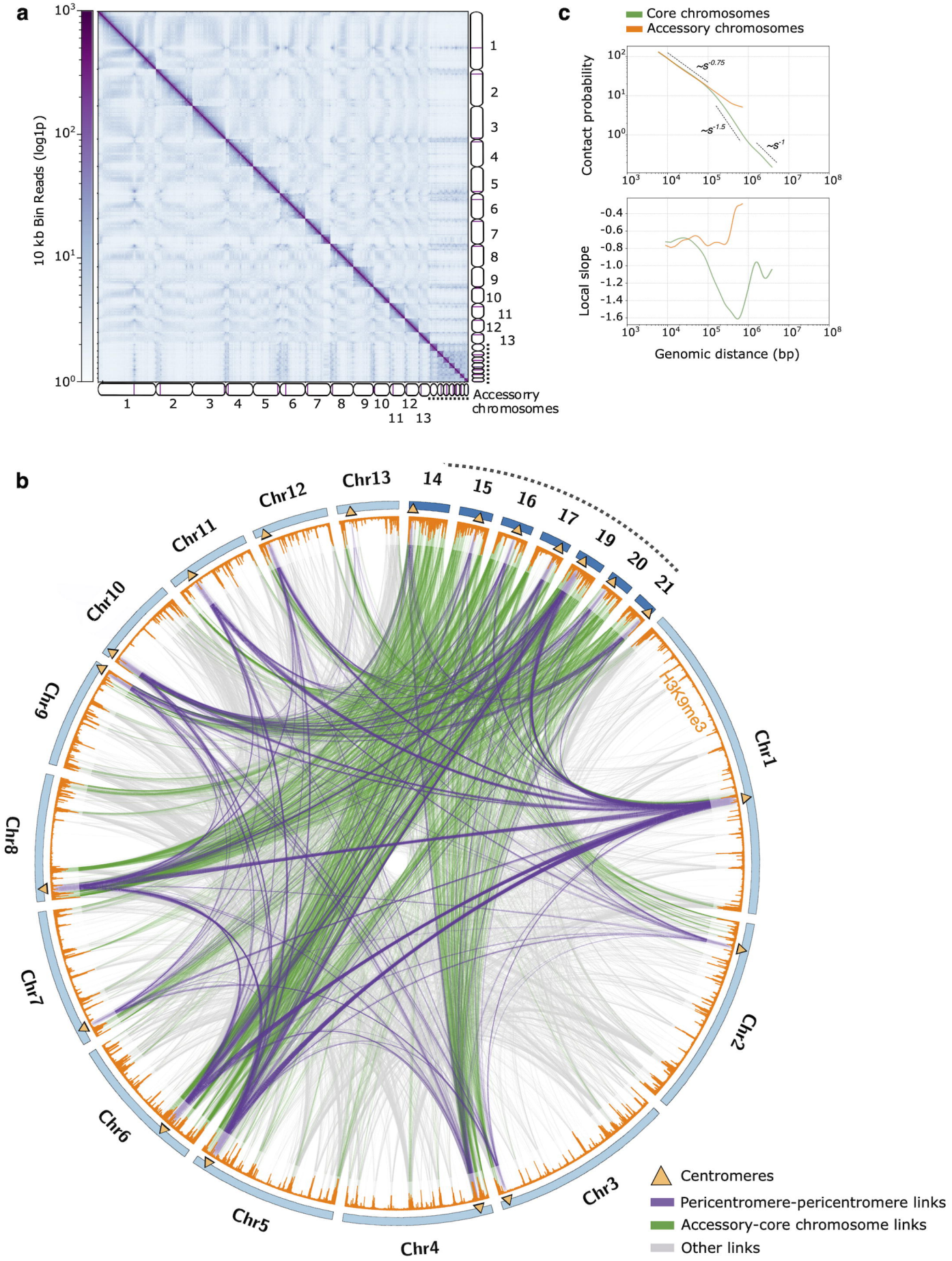
a
10 kb Bin Reads (log1p)
Accessorry chromosomes
b
Chr1
Chr2
Chr3
Chr4
Chr5
Chr6
Chr7
Chr8
Chr9
Chr10
Chr11
Chr12
Chr13
14
15
16
17
19
20
21
H3K9me3
Centromeres
Pericentromere-pericentromere links
Accessory-core chromosome links
Other links
c
Core chromosomes
Accessory chromosomes
Contact probability
Local slope
Genomic distance (bp)

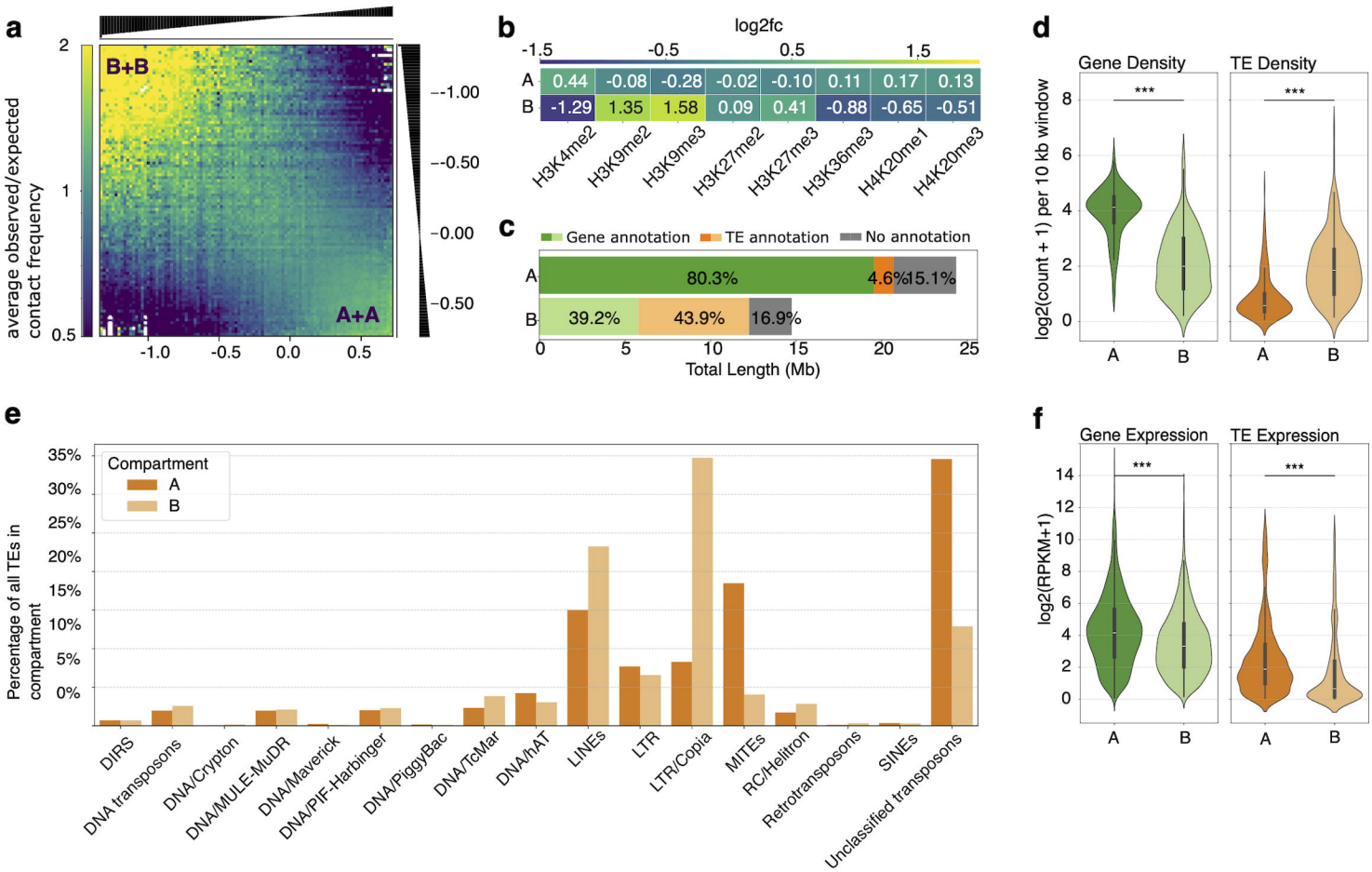
a
B+B
A+A
average observed/expected contact frequency
b
log2fc
A 0.44 -0.08 -0.28 -0.02 -0.10 0.11 0.17 0.13
B -1.29 1.35 1.58 0.09 0.41 -0.88 -0.65 -0.51
H3K4me2
H3K9me2
H3K9me3
H3K27me2
H3K27me3
H3K36me3
H4K20me1
H4K20me3
c
Gene annotation
TE annotation
No annotation
A 80.3% 4.6% 15.1%
B 39.2% 43.9% 16.9%
Total Length (Mb)
d
Gene Density
TE Density
log2(count + 1) per 10 kb window
e
Compartment
A
B
Percentage of all TEs in compartment
DIRS
DNA transposons
DNA/Crypton
DNA/MULE-MuDR
DNA/Maverick
DNA/PIF-Harbinger
DNA/PiggyBac
DNA/TcMar
DNA/hAT
LINEs
LTR
LTR/Copia
MITEs
RC/Helitron
Retrotransposons
SINEs
Unclassified transposons
f
Gene Expression
TE Expression
log2(RPKM+1)

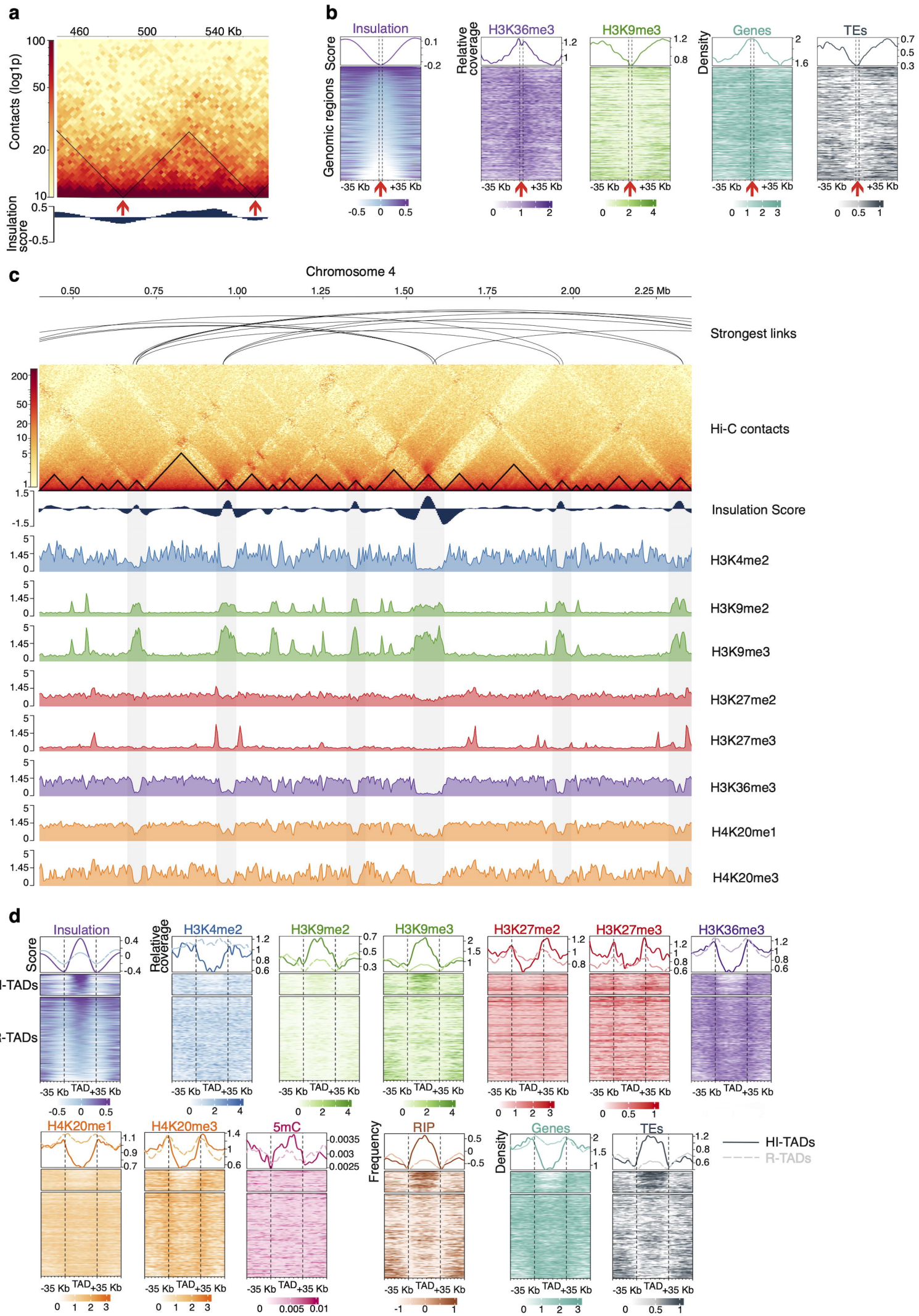
a
460
500
540 Kb
Contacts (log1p)
Insulation score
b
Insulation
Score
Genomic regions
H3K36me3
Relative coverage
H3K9me3
Genes
Density
TEs
-35 Kb
+35 Kb
c
Chromosome 4
0.50
0.75
1.00
1.25
1.50
1.75
2.00
2.25 Mb
Strongest links
Hi-C contacts
Insulation Score
H3K4me2
H3K9me2
H3K9me3
H3K27me2
H3K27me3
H3K36me3
H4K20me1
H4K20me3
d
Insulation
Score
HI-TADs
R-TADs
H3K4me2
Relative coverage
H3K9me2
H3K9me3
H3K27me2
H3K27me3
H3K36me3
-35 Kb
TAD
+35 Kb
H4K20me1
H4K20me3
5mC
RIP
Frequency
Genes
Density
TEs
HI-TADs
R-TADs